Appl Phys B (2009) 95: 245–259
DOI 10.1007/s00340-009-3431-1

Applied Physics B
Lasers and Optics

Photoelectron angular distributions from strong-field coherent electronic excitation

M. Wollenhaupt · M. Krug · J. Köhler · T. Bayer · C. Sarpe-Tudoran · T. Baumert

Received: 2 October 2008 / Revised version: 5 February 2009 / Published online: 27 February 2009

Abstract Photoelectron Angular Distributions (PADs) resulting from nonperturbative excitation of potassium atoms using shaped femtosecond laser pulses are presented. We study control exerted by (1) the polarization of an unshaped, i.e., a bandwidth-limited light pulse, (2) shaped linearly polarized light, and (3) a combination of both degrees of freedom, i.e., polarization-shaped laser pulses. A theoretical approach to describe PADs from nonperturbative Resonance Enhanced Multi-Photon Ionization (REMPI) with ultrashort polarization-shaped laser pulses is presented and compared to experimental results. Applications of this technique to the generation and observation of atomic ring currents are discussed.

PACS 32.80.Qk · 32.80.Rm · 33.80.Rv

1 Introduction

The experimental realization of shaped ultrashort laser fields [1, 2] is at the heart of coherent control. Control scenarios ranging from "open-loop" quantum interference on model systems to adaptive control schemes applied to systems with ever increasing complexity [3–13] have been studied theoretically and demonstrated experimentally. In these experiments, highly structured—but in most cases linearly polarized—femtosecond laser pulses have been employed to control light-induced dynamics of quantum systems. Recently, with the advent of pulse shapers that are capable of generating complex shaped time-dependent polarization profiles in addition [14–19], experimental demonstrations of quantum control by making use of polarization-shaping as additional degree of freedom [20–23] have been presented. Another degree of freedom in quantum control is accessible by intense laser fields. In those fields the light–matter interaction is highly nonperturbative and gives rise to level-shifts in the order of hundreds of meV due to AC–Stark shifts. Strong-field coherent control has been demonstrated by dynamic Stark splitting of resonances [24–27] and nonresonant Stark shifts of molecular potentials [28, 29].

In this contribution, we present a coherent control scenario making use of nonperturbative control by intense polarization-shaped laser pulses. In particular, we extend earlier studies on coherent control of electronic excitation by shaped linearly polarized light to nonperturbative light–matter interaction using polarization-shaped laser pulses and detection by Photoelectron Angular Distributions (PAD). Our previous strong-field experiments have been interpreted in terms of Selective Population of Dressed States (SPODS) [30, 31], which provides a unifying framework for established strong-field mechanisms such as Photon Locking (PL) [32–34] by temporal phase discontinuities and Rapid Adiabatic Passage (RAP) [35] by chirped pulses. Realizations of SPODS were demonstrated by using pulse sequences [24, 36], shaped pulses such as sinusoidally phase-modulated pulses [37, 38], chirped pulses [39], and combinations thereof [40, 41]. Physical pictures to describe the mechanism of SPODS involve bare states dynamics [24], dressed states dynamics [30], dynamics of the Bloch-vector [11, 38, 39], and recently a spatio-temporal picture considering the dynamics of coherent electronic wave packets in shaped laser fields [40]. In that contribution, wave packets made of superpositions of $|s, m = 0\rangle$ and $|p, m = 0\rangle$

M. Wollenhaupt (✉) · M. Krug · J. Köhler · T. Bayer · C. Sarpe-Tudoran · T. Baumert
Institut für Physik und CINSaT, Universität Kassel, Heinrich-Plett-Str. 40, 34132 Kassel, Germany
e-mail: wollenha@physik.uni-kassel.de

states were produced and manipulated by linearly polarized shaped pulses, and the transient dynamics was mapped by simultaneous ionization. An alternative approach to observe coherent transients from shaped femtosecond excitation of atoms by pump–probe techniques was initially reported in [42] and recently applied to photoassociation of ultracold molecules [43]. In this contribution we report on $1+2$ Resonance Enhanced Multi-Photon Ionization (REMPI) experiments employing polarization-shaped laser pulses to (1) control electronic wave packets in the neutral atom as a model system for controlled (neutral) molecular dynamics and (2) exert control on free-electron wave packets by multi-photon ionization. In the first step polarization-shaped pulses are used to excite tailored superpositions of the $|s, m=0\rangle$ and $|p, m=\pm 1\rangle$ electronic states. In the second step multi-photon ionization with photons of specifically tailored polarization allows us to exert control over a whole manifold of electronic states such as the *virtual* $|d, m=0\rangle$ and $|d, m=\pm 2\rangle$ states as well as the final free $|f, m=\pm 1\rangle$ and $|f, m=\pm 3\rangle$ states. In general, as exemplified above, tailoring the state of polarization gives access to controlling angular momenta and—associated with this—the ability to shape the angular distributions of matter waves. In our experiment we shape ultrashort *free electron wave packets* [44] by ultrashort polarization-shaped laser pulses. Detection of PADs [45, 46] is the adequate technique to directly map the spatial facet of coherent strong-field electronic excitation by ultrashort polarization-shaped laser pulses and thereby help us to unravel strong-field dynamics induced by polarization-shaped light. Combining polarization-shaping with detection of PADs has high potential for novel applications such as the observation of controlled dynamics of chiral molecules, the characterization of attosecond dynamics and the generation and detection of atomic ring currents [47]. Initial experimental results relevant to atomic ring currents are also presented in this contribution.

Our contribution is organized as follows. We will start in Sect. 2 with the theoretical description of polarization-shaped laser fields and their interaction with atomic quantum systems. Strong-field neutral excitation and perturbative multi-photon ionization of potassium atoms are discussed consecutively in order to derive a handling of both the radial and the angular distribution of emitted photoelectrons. In Sect. 3, our experimental apparatus is described, including the polarization pulse shaper and the photoelectron imaging spectrometer. Section 4 gives the results obtained from interaction of potassium atoms with the unmodulated pulse, purely phase-shaped pulses and, finally, with complex polarization-shaped laser pulses. We end this article with a brief summary and conclusions.

2 Theory

In this section, we describe $1+2$ REMPI of atoms by ultrashort laser pulses with an arbitrary instantaneous state of polarization detected by PADs loosely following the notation of [48] and [49]. To this end, we introduce the laboratory frame coordinate system in which the (time-dependent) polarization vector $\hat{\boldsymbol{\epsilon}}(t)$ of the laser pulse propagating along the z-axis is located in the x–y-plane (see Fig. 3(e) for a sketch of the coordinate system). PADs are generated by acceleration of the electrons in x-direction. In the following sections we start by introducing polarization-shaping in the frequency domain specifically adapted to describing the interaction of ultrashort polarization-shaped laser pulses with atoms. Subsequently, one-photon strong-field interaction in neutral potassium atoms is looked at by solving the time-dependent Schrödinger equation. Simultaneous multi-photon ionization of the interacting system is treated perturbatively, yielding three-dimensional free-electron wave packets. PADs are obtained by projecting these wave packets onto a two-dimensional detector plane.

2.1 Polarization-shaping

In view of a consistent *quantum mechanical* description of the light–atom interaction given below, the electric field is described in terms of its (negative frequency) analytical signal $\mathcal{E}^-(t)e^{-i\omega_0 t}$ characterized by the complex valued envelope $\mathcal{E}^-(t)$ and oscillating at the central frequency of the laser radiation ω_0. The positive frequency analytical signal customarily used in femtosecond optics [1, 2] is related to our notation by $\mathcal{E}^+(t)=[\mathcal{E}^-(t)]^*$. In order to simplify the notation, the superscript "−" is omitted throughout the remainder of this article. Fourier-transform of the envelope delivers the spectrum $\tilde{\mathcal{E}}(\omega)$. Independent spectral phase-shaping of two orthogonal linearly polarized components of $\tilde{\mathcal{E}}(\omega)$ by the phase functions $\varphi_x(\omega)$ and $\varphi_y(\omega)$

$$\begin{pmatrix}\tilde{\mathcal{E}}_{x,\mathrm{mod}}(\omega)\\ \tilde{\mathcal{E}}_{y,\mathrm{mod}}(\omega)\end{pmatrix}=\tilde{\mathcal{E}}(\omega)\begin{pmatrix}e^{i\varphi_x(\omega)}\\ e^{i\varphi_y(\omega)}\end{pmatrix} \tag{1}$$

yields two linearly polarized modulated spectral light fields $\tilde{\mathcal{E}}_{x,\mathrm{mod}}(\omega)$ and $\tilde{\mathcal{E}}_{y,\mathrm{mod}}(\omega)$ resulting in the shaped temporal fields $\mathcal{E}_{x,\mathrm{mod}}(t)$ and $\mathcal{E}_{y,\mathrm{mod}}(t)$ obtained by inverse Fourier-transform. A more detailed characterization of the experimental implementation of the polarization-shaper is given in Sect. 3.2. In order to describe the light–atom interaction of a laser electric field being in a state of arbitrary polarization, it is advantageous to decompose the field into superpositions of left-handed $\mathcal{E}_L(t)$ and right-handed $\mathcal{E}_R(t)$ circularly polarized shaped light pulses

$$\begin{pmatrix}\mathcal{E}_L(t)\\ \mathcal{E}_R(t)\end{pmatrix}=\frac{1}{\sqrt{2}}\begin{pmatrix}\mathcal{E}_x(t)-i\mathcal{E}_y(t)\\ \mathcal{E}_x(t)+i\mathcal{E}_y(t)\end{pmatrix}, \tag{2}$$

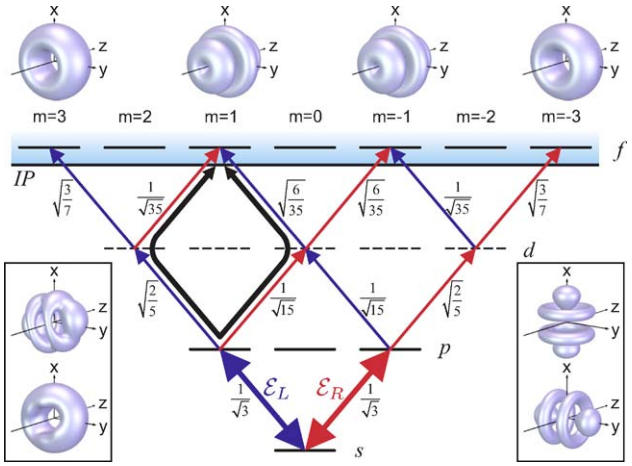

Fig. 1 Scheme for $1+2$ REMPI of potassium atoms by laser light with an arbitrary state of polarization arising from superpositions of left-handed $\mathcal{E}_L(t)$ and right-handed $\mathcal{E}_R(t)$ circularly polarized shaped light propagating along the z-axis. *Bold double-headed arrows* indicate the nonperturbative excitation of the one-photon $p \leftrightarrow s$ transitions. Perturbative two-photon ionization $f \leftarrow\!\leftarrow p$ via eight different pathways through the *virtual* $|d, m\rangle$ states (indicated with *dashed lines*) gives rise to free-electron wave packets with an energy above the ionization potential (*IP*) and $|f, m = \pm 3\rangle$ and $|f, m = \pm 1\rangle$ symmetry. Coherent superposition of these continuum states can produce electron probability distributions with (rotated) $|f, m = 0\rangle$ symmetry. The rotation angle of the $|f, m = 0\rangle$ wave packet about the z-axis is determined by the relative phases of $\mathcal{E}_L(t)$ and $\mathcal{E}_R(t)$ exemplified for an alignment parallel to either the x- or y-axis (*right panel*). Elliptically polarized light produces superposition states as indicated in the *left panel*. For convenience, the relative transition moments $\alpha_{l,m;l',m'}$ are indicated for each transition. In this special case the two contributions to, e.g., $c_{3,\pm 1}(\omega_e)$ are identical as indicated with the two *black bended arrows*

where the subscript *mod* for modulated fields is suppressed for better readability. Note that any instantaneous state of polarization is described by this decomposition, provided that the appropriate relative (time-dependent) phase between these fields is taken into account.

2.2 Non-perturbative interaction in the neutral system

As the laser radiation propagates in the z-direction and the light field is decomposed into two circularly polarized components, only $\Delta m = \pm 1$ transitions shown in Fig. 1 take part in the light–matter interaction [48] (details of the excitation scheme relevant to the experiment are shown in Fig. 4). Therefore, nonperturbative excitation of the one-photon transitions $p_{+1} \leftrightarrow s$ and $p_{-1} \leftrightarrow s$ (see bold double-headed arrows in Fig. 1) is described by the time-dependent Schrödinger equation

$$\frac{d}{dt}\begin{pmatrix} s(t) \\ p_{+1}(t) \\ p_{-1}(t) \end{pmatrix} = i \begin{pmatrix} 0 & \frac{\Omega_L^*(t)}{2} & \frac{\Omega_R^*(t)}{2} \\ \frac{\Omega_L(t)}{2} & \delta_{+1} & 0 \\ \frac{\Omega_R(t)}{2} & 0 & \delta_{-1} \end{pmatrix} \begin{pmatrix} s(t) \\ p_{+1}(t) \\ p_{-1}(t) \end{pmatrix}, \qquad (3)$$

where $\hbar\Omega_{L/R}(t) = \mu_{L/R}\,\mathcal{E}_{L/R}(t)$ and $\mu_{L/R}$ describe the Rabi-frequencies and the dipole moments of the respective transitions, $\delta_{\pm 1}$ the detunings of the $|p, m = \pm 1\rangle$ states with respect to the laser central frequency, and $\{s(t),\, p_{+1}(t),\, p_{-1}(t)\}^T$ the state vector in terms of the corresponding time-dependent amplitudes [11, 35, 38, 49]. Note that in this simplified scheme the influence of the spin has been ignored, because the fine structure splitting of the $4p$-state into $4p_{1/2}$- and $4p_{3/2}$-states of about 7 meV is small compared to the laser bandwidth of about 60 meV Full Width at Half Maximum (FWHM) for a 30 fs laser pulse. Here, both detunings from the laser central frequency are taken to be identical, i.e., $\delta_{+1} = \delta_{-1}$. However, the form of the Hamiltonian chosen in (3) is also applicable in the general case of different detunings.

2.3 Perturbative two-photon ionization

2.3.1 Angular part

Since the dipole moments for neutral-to-ionic transitions are generally much weaker compared to, for instance, the potassium D-line, two-photon ionization from the two p-states is treated by time-dependent perturbation theory. The description based on $\Delta m = \pm 1$ transitions as outlined above will also be used to describe two-photon ionization. However, especially for REMPI with linearly polarized pulses, it is more natural to switch into the *atomic frame* [50] and describe the interaction by $\Delta m = 0$ transitions *in the atomic frame*, as if a hypothetical laser pulse propagated along a direction in the x–y-plane. This amounts to rotating the actual $|f, m = 0\rangle$ wave function by 90° about the y-axis and subsequently by an arbitrary angle about the z-axis. Although both the $f \leftarrow\!\leftarrow p$ and $p \leftarrow\!\leftarrow p$ two-photon transitions are allowed from selection rules, the contributions from the free-electron wave packets with $|p, m = \pm 1\rangle$ symmetry are hardly visible in the experimental observations (see Sect. 4). Therefore, we consider two-photon ionization $f \leftarrow\!\leftarrow p$ via the eight different pathways through the *virtual* $|d, m\rangle$ states as indicated in Figs. 1 and 4 giving rise to free-electron wave packets with $|f, m = \pm 3\rangle$ and $|f, m = \pm 1\rangle$ symmetry. Coherent superposition of these continuum states can produce electron probability distributions with $|f, m = 0\rangle$ symmetry *in the atomic frame*. The $|f, m = 0\rangle$ wave packet is aligned in the x–y-plane, and its rotation angle about the z-axis is determined by the relative phases of $\mathcal{E}_L(t)$ and $\mathcal{E}_R(t)$. Examples for two such states aligned parallel to either the x- or y-axis are shown in the right inset to Fig. 1. Elliptically polarized light produces highly structured superposition states with additional features as indicated in the left inset.

For quantitative description, the relative transition moments due to the angular part of the wave functions

$$\alpha_{l,m;l',m'} = \hat{\boldsymbol{\epsilon}}_{L/R} \cdot \langle l, m|\hat{\boldsymbol{x}}|l', m'\rangle \qquad (4)$$

as indicated in Fig. 1 for each transition need to be considered. The radial parts, however, are identical for all pathways. In (4), $\hat{\boldsymbol{x}}$ denotes the position operator, and

$$\hat{\boldsymbol{\epsilon}}_L = \frac{1}{\sqrt{2}}\begin{pmatrix}1\\ i\end{pmatrix} \quad \text{and} \quad \hat{\boldsymbol{\epsilon}}_R = \frac{1}{\sqrt{2}}\begin{pmatrix}1\\ -i\end{pmatrix} \tag{5}$$

are the basis vectors for left- and right-handed circularly polarized light. The relative weight for each ionization pathway is proportional to the product of the transition moments $\alpha_{l,m;l',m'}$ and the electric field $\mathcal{E}_{L/R}(t)$ for *both* photons, i.e., each (two-photon) pathway contributes an amplitude proportional to

$$\alpha_{l,m;l',m'}\,\mathcal{E}_{L/R}(t)\,\alpha_{l',m';l'',m''}\,\mathcal{E}_{L/R}(t). \tag{6}$$

2.3.2 Kinetic energy distribution

Using second-order perturbation theory, the amplitude $c_{3,3}(\omega_e)$ for photoelectrons with a kinetic energy of $E_{\mathrm{kin}} = \hbar\omega_e$ and $|f, m = 3\rangle$ symmetry reads

$$c_{3,3}(\omega_e) \propto \alpha_{1,1;2,2}\,\alpha_{2,2;3,3} \int p_{+1}(t)\left[\mathcal{E}_L(t)\right]^2 e^{i\delta\omega_e t}\,dt \tag{7}$$

with $\delta\omega_e = \omega_e + \omega_{IP} - \omega_p - 2\omega_0$ [11, 24, 38, 44], where $\hbar\omega_{IP}$ and $\hbar\omega_p$ denote the ionization energy and the energy of the p-states, respectively. In this simple case there is only one ionization path contributing to photoelectrons with $|f, m = 3\rangle$ symmetry. In general, all interfering pathways leading to the same final state need to be taken into account. For example, three pathways contribute to PADs with $|f, m = 1\rangle$ symmetry, and therefore the energy dependence of the amplitudes is described by

$$\begin{aligned} c_{3,1}(\omega_e) &\propto \alpha_{1,1;2,2}\,\alpha_{2,2;3,1} \int p_{+1}(t)\,\mathcal{E}_L(t)\mathcal{E}_R(t) e^{i\delta\omega_e t}\,dt \\ &+ \alpha_{1,1;2,0}\,\alpha_{2,0;3,1} \int p_{+1}(t)\,\mathcal{E}_R(t)\mathcal{E}_L(t) e^{i\delta\omega_e t}\,dt \\ &+ \alpha_{1,-1;2,0}\,\alpha_{2,0;3,1} \int p_{-1}(t)\left[\mathcal{E}_L(t)\right]^2 e^{i\delta\omega_e t}\,dt. \end{aligned} \tag{8}$$

In this special case the first two contributions to $c_{3,1}(\omega_e)$ are identical as indicated with the two black bended arrows in Fig. 1.

2.3.3 Photoelectron angular distributions

Describing the angular part of the electron wave functions by spherical harmonics $Y_{l,m}(\theta, \phi)$ and the energy dependence by the amplitudes $c_{l,m}(\omega_e)$, the electron wave functions with $|l, m\rangle$ symmetry result in

$$\psi_{l,m}(E_{\mathrm{kin}}, \theta, \phi) = c_{l,m}(\omega_e) \cdot Y_{l,m}(\theta, \phi). \tag{9}$$

Coherent superposition of all contributions for a given l quantum number yields the total wave function

$$\psi_l(E_{\mathrm{kin}}, \theta, \phi) = \sum_m \psi_{l,m}(E_{\mathrm{kin}}, \theta, \phi), \tag{10}$$

i.e., the probability for the observation of an electron with kinetic energy E_{kin} at the angles θ and ϕ is

$$p(E_{\mathrm{kin}}, \theta, \phi) = \left|\psi_l(E_{\mathrm{kin}}, \theta, \phi)\right|^2. \tag{11}$$

Because the free-electron wave packet evolves into its kinetic energy distribution in *coordinate* space, $p(E_{\mathrm{kin}}, \theta, \phi)$ describes the three-dimensional wave packet as measured by a spatial detector. A detailed analysis of the time evolution of the Wigner phase-space distribution of a free-electron wave packet reveals how the wave packet evolves from its initial state into its *energy* or *momentum* distribution in *coordinate* space [51]. The PAD as measured on a planar detector oriented in the y–z-plane is obtained by Abel-transform of the probability distribution along the x-axis [45, 46].

2.4 Results from the numerical simulation

With the *ansatz* described above PADs are simulated for physically transparent situations in order to provide a clear picture of the control scenarios accessible in strong-field control by polarization-shaped light fields. To this end, we consider two limiting cases disentangling the influence of strong-field excitation from polarization effects. In the first scenario we consider the effect of the nonperturbative character of the excitation process on the PADs. In the second case the influence of the polarization on PADs is studied by controlling the relative *amplitudes and phases* of the left and right circularly polarized light fields $\mathcal{E}_L$ and $\mathcal{E}_R$.

2.4.1 Control by strong fields

In general, nonperturbative excitation by shaped pulses is responsible for strong-field dynamics such as Rabi-oscillations [52], Rapid Adiabatic Passage [35, 39, 53, 54], or Photon Locking [32, 33, 55, 56]. The dynamics in three-level systems induced by shaped laser radiation as described by (3) is even more comprehensive. The excited states dynamics is captured by the amplitudes $p_{+1}(t)$ and $p_{-1}(t)$. As a consequence, strong-field effects will be mapped into the energy-dependent photoionization probability $c_{l,m}(\omega_e)$ in virtue of (7) and (2.3.2), and therefore, manifest themselves in the radial distribution of the PAD. As an example, PADs are simulated for resonant excitation with $\mathcal{E}_L = -\mathcal{E}_R$ corresponding to linear polarization along the y-axis as shown in Fig. 2. All PADs presented in this contribution are coded in a false color representation using the mapping indicated by the color bar in Fig. 2. The PADs correspond to electron

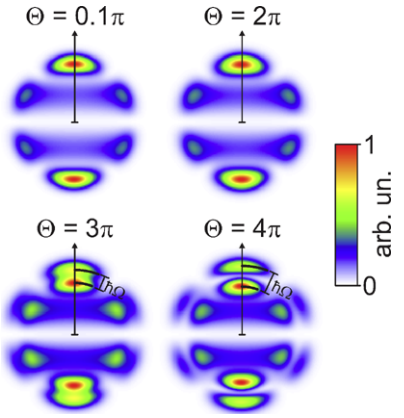

Fig. 2 Simulated PADs for resonant excitation with $\mathcal{E}_L = -\mathcal{E}_R$ corresponding to linear polarization along the y-axis resulting in a photoelectron distribution with $|f, m = 0\rangle$ symmetry *in the atomic frame*. With increasing pulse area from $\Theta = 0.1\pi$ to $\Theta = 4\pi$ the AT-splitting $\hbar\Omega$ exceeds the laser bandwidth and becomes more visible. All false color representations use the mapping indicated by the *color bar*

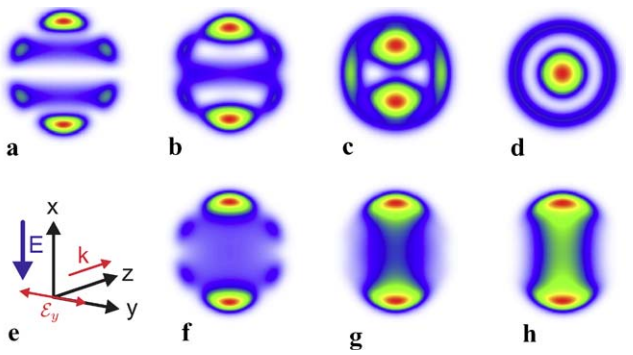

Fig. 3 Simulated PADs for $\Theta = 2\pi$ pulses. Upper panels: $\mathcal{E}_L = -\mathcal{E}_R$, with relative phases of (**a**) 0, (**b**) $\pi/3$, (**c**) $2\pi/3$, and (**d**) π ($\mathcal{E}_L = \mathcal{E}_R$) corresponding to light pulses linearly polarized with an angle of 0°, 30°, 60°, and 90° with respect to the y-axis (compare to the experimental PADs in Fig. 10(a)–(d)). *Lower panels left*: (**e**) sketch of the coordinate system for the simulation. The extraction field E along the x-axis determines the direction of the Abel-transform and the k-vector along the z-axis describes the light propagation direction. $\mathcal{E}_y$ describes light polarized along the y-axis. *Lower panels right*: variation of the relative *amplitude and phase* of the left and right circularly polarized light fields mimicking the effect of elliptically polarized light from a $\lambda/4$ plate with retardation axis oriented at (**f**) 15°, (**g**) 30°, and (**h**) 45° with respect to the y-axis (compare with the experimental PADs in Fig. 10 (e)–(h))

wave packets with an $|f, m = 0\rangle$ symmetry *in the atomic frame* and show pronounced Autler–Townes-splitting (AT-splitting) due to Rabi-oscillations. In the perturbative limit, i.e., for a pulse area of $\Theta = 0.1\pi$, the width of the photoelectron spectra is determined by the bandwidth of the laser radiation. As Θ increases, the AT-splitting of $\hbar\Omega$ increases in the same manner. At $\Theta = 2\pi$ the photoelectron spectrum is slightly broadened, but the AT-splitting is hardly visible. For higher intensities, i.e., at $\Theta = 3\pi$ and $\Theta = 4\pi$, the AT-splitting exceeds the laser bandwidth and provides the evidence for nonperturbative excitation, including the preparation of a (transient) superposition state of maximum coherence.

2.4.2 Control by polarization

Polarization-dependent PADs are studied by variation of the relative *amplitudes and phases* of left and right circularly polarized light $\mathcal{E}_L$ and $\mathcal{E}_R$ (see Fig. 3). The pulse area of $\Theta = 2\pi$ was chosen to study the PAD resulting from nonperturbative excitation not yet influenced by AT-splitting (cf. Fig. 2). In the upper panels of Fig. 3 linearly polarized light with an angle of 0°, 30°, 60°, and 90° with respect to the y-axis is mimicked by setting $\mathcal{E}_L = -\mathcal{E}_R$ and the relative phases of the two polarization components to (a) 0, (b) $\pi/3$, (c) $2\pi/3$, and (d) π. The lower panels of Fig. 3 show PADs from elliptically polarized $\Theta = 2\pi$ pulses corresponding to the effect of a $\lambda/4$ plate with retardation axis oriented at angles of (f) 15°, (g) 30°, and (h) 45° with respect to the y-axis, simulated by variation of the relative *amplitude and the relative phase* of both polarization components.

3 Experimental

In our experiments, we combine polarization pulse-shaping techniques with measurements of PADs resulting from excitation of potassium atoms. In this section, we start by introducing the potassium excitation and ionization scheme. Subsequently we present the setup of our polarization pulse shaper including a discussion about experimental aspects regarding the accurate generation of shaped laser pulses with a well-defined time-dependent polarization profile. We end this section by describing the layout of our photoelectron imaging spectrometer.

3.1 Excitation scheme

Figure 4 shows the excitation scheme of potassium atoms. All levels are plotted using energies obtained from the NIST-database [57]. In the first step non-perturbative excitation into the $4p$-states (corresponding to 768 nm) is accomplished using a laser pulse with a slightly red–detuned spectrum ($\lambda_0 = 795$ nm) of sufficiently large bandwidth (60 meV FWHM). Further dipole-allowed resonant transitions are not available, because the transition to the $5p$-state is dipole-forbidden and the dipole-allowed states $5s$, $6s$, $3d$, and $4d$ are strongly detuned by more than 280 meV from the available excitation energy. Thus two-photon ionization proceeds via an intermediate *virtual* state. The main ionization pathway (solid arrows in Fig. 4) leads to free-electron wave packets with $|f\rangle$ symmetry. Wave packets with $|p\rangle$ symmetry resulting from alternative ionization pathways (dashed

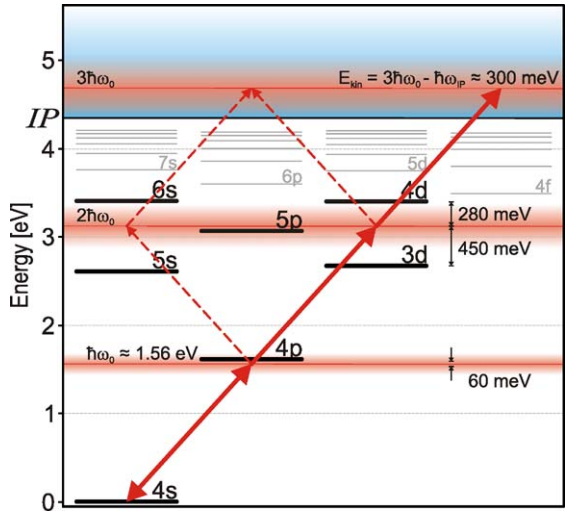

Fig. 4 Excitation scheme of potassium atoms. The main ionization pathway is illustrated by *solid arrows*. The transition from the $4s$- to $4p$-state, resonant at about 768 nm, lies within the laser bandwidth (60 meV FWHM) visualized by the corresponding bar with color gradient. The multi-photon spectra are represented by expanding bars correlated with the range of available multi-photon energies. In this REMPI process, the central kinetic energy of the photoelectrons E_{kin} above the *IP* is about 300 meV determined by $3\hbar\omega_0 - \hbar\omega_{IP}$. Alternative ionization pathways leading to contributions of free-electron wave packets with $|p, m = \pm 1\rangle$ symmetry are indicated with *dashed arrows*. All levels are plotted using energies obtained from the NIST-database

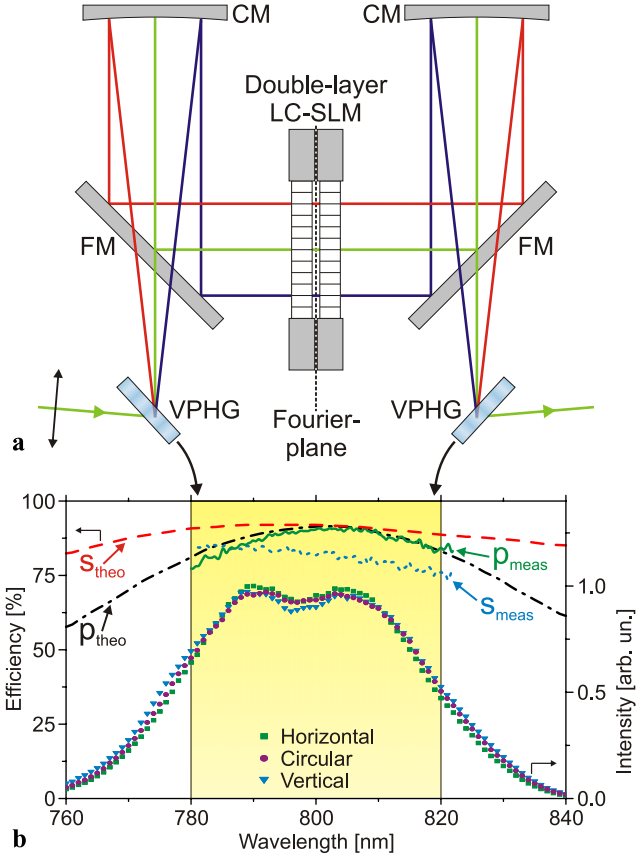

Fig. 5 (**a**) Schematic layout of the polarization pulse shaper consisting of a $4f$-setup and a double-layer LC-SLM. The setup provides minimal tilting angles and optical errors (on-axis reflection for the cylindrical mirrors). The *black double-headed arrow* shows the linear polarization state of light entering the pulse shaper. VPHG: Volume Phase Holographic Grating, CM: Cylindrical Mirror (focal length 223 mm), FM: Planar Folding Mirror. (**b**) Diffraction efficiencies of the Volume Phase Holographic Gratings for p- and s-polarized light. Measured and theoretical values are labeled by the subscripts *meas* and *theo*, respectively. In addition, spectra of pulses having different polarization states (horizontal, circular, vertical) generated by applying the corresponding phase functions to the LC-SLM are shown. Within the measurement accuracy they confirm the nearly polarization-independent transmission properties of our experimental setup as expected from the efficiency curves

arrows in Fig. 4) contribute very weakly and are hardly observed in the experiment. In this REMPI process, the average kinetic energy of the photoelectrons E_{kin} above the ionization potential (*IP*) is about 300 meV determined by the excess energy $3\hbar\omega_0 - \hbar\omega_{IP}$.

3.2 Polarization pulse shaper

Our home-built high-resolution polarization pulse shaper (0.16 nm/pixel at 800 nm) is based on a previous design of a compact and robust phase-only modulator [58]. It consists of a double-layer Liquid Crystal Spatial Light Modulator (LC-SLM) located in the Fourier-plane of a $4f$-zero dispersion compressor (Fig. 5(a)). The preferential orientation axes of the LCs in the two layers of the 2×640 pixel SLM (*Jenoptik SLM–S640d*) are rotated by $\pm 45°$ with respect to the polarization direction of the incident linearly polarized light allowing for simultaneous and independent spectral phase modulations of two orthogonal polarization components. By the use of Volume Phase Holographic Gratings (*Wasatch Photonics*, 1840 lines/mm) high diffraction efficiencies and large bandwidths, i.e., flat efficiency curves are obtained (Fig. 5(b)). For both p (horizontally) and s (vertically)-polarized light the gratings possess efficiency values higher than 75% in the range of 780 to 820 nm. This results in a total pulse shaper transmission of more than 30% (50%) for 30 fs (50 fs) pulses.

Accurate generation of polarization-shaped femtosecond laser pulses, i.e., pulses with a well-defined time-dependent polarization profile, is very challenging in the laboratory, because it may suffer from several experimental conditions [59]. In the following we explain our procedure to assure that the shaped pulses used in the experiments do not significantly differ from the pulses theoretically estimated from the phase functions inscribed on the pulse shaper's LC-SLM. In the first step we optimize the initial pulses for subsequent pulse shaping. To this end, we characterize the pulses by a spectrogram-based method [60], before sending them into the photoelectron imaging spectrometer. The dispersion of the optical components in the beam path including the

imaging spectrometer's entrance window is compensated by the use of a prism compressor, resulting in bandwidth-limited pulses of 30 fs duration. Prior to the experiments, we carefully adjusted our polarization pulse shaper for realization of a dispersion-free 4 f-setup. By passing through the pulse shaper the 30 fs input pulses are stretched to about 45 fs due to the shaper's spectral transmission characteristics. Both layers of our LC-SLM have been carefully calibrated employing a standard method similar to the one described in [1]. Small differences in the calibration curves between the two layers along with the dispersion properties of the LCs are taken into account when phase functions are applied to the LC-SLM. The generation of circularly polarized light is one of the most challenging tasks for a polarization pulse shaper, because even small residual phase and amplitude modulations distort the desired polarization profile significantly. First, we show that no significant polarization-dependent *amplitude modulations* are introduced by the device. To this end, we consider spectra of pulses being in horizontal, circular, and vertical polarization states generated by applying the corresponding phase functions to the LC-SLM layers as shown in Fig. 5(b). The agreement of the three spectra indicates that the transmission properties of our pulse shaper are nearly polarization-independent. Undesired *phase shifts* between the p- and s-polarized field components in our setup were investigated employing a simple optical scheme. Again, spectra of horizontally, circularly, and vertically polarized pulses generated using the polarization pulse shaper have been measured after passing a rotatable analyzer. These measurements provide a spectrally resolved polarization state analysis. Figure 6(a) presents the simulated results for the three different polarization states. The simulation is based on the pulse shaper's input spectrum assuming that no polarization and no wavelength-dependent amplitude modulations and in particular no undesired phase shifts are present. In the case of horizontally polarized light maxima for all spectral components are observed for analyzer orientations of 0°, 180°, and 360°, the minima are shifted by 90° and lie at angles of 90° and 270°. For vertically polarized light maxima and minima are exchanged. In the special case of circular polarization, the spectrally resolved intensities are constant, i.e., independent of the analyzer orientation. In Fig. 6(b) the results of the experimental polarization state and, hence, phase shift analysis are shown. For horizontally and vertically polarized light, only slight differences in comparison to the simulation are visible. The main effect observed is a reduction of the bandwidth due to the spectral transmission properties of the pulse shaper resulting from the diffraction efficiencies of the VPHGs (cf. Fig. 5). In contrast to the constant signal in the simulation, the experimental results for circular polarization exhibit a periodic structure with maxima and minima revealing the presence of

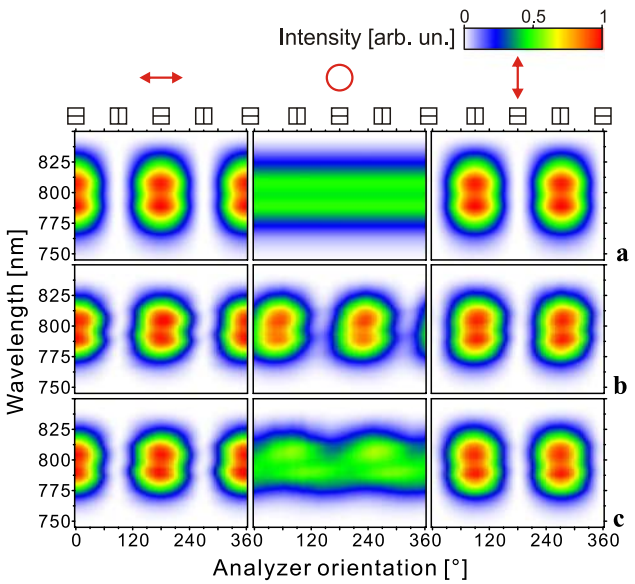

Fig. 6 Spectrally resolved polarization state analysis for investigation of possible phase shifts between p- and s-polarized field components. Spectra of pulses being in different polarization states (horizontal, circular, vertical) are measured after passing a rotatable analyzer as a function of the analyzer orientation (*squares*). (**a**) Simulation results based on the pulse shaper's input spectrum assuming that no polarization and no wavelength-dependent amplitude modulations and, in particular, no phase shifts are present. For horizontally and vertically polarized light maxima and minima are visible, while for circular polarization, a constant signal is expected. (**b**) Results of the experimental polarization state and, hence, phase shift analysis. Especially for circularly polarized light, differences to the simulation are found. These deviations reveal the presence of undesired phase shifts leading to a modification of the desired polarization state. (**c**) Measurement results obtained by making use of a Berek-compensator for correction of the detected phase shifts. Successful compensation is demonstrated by the essentially constant spectra measured for circularly polarized light

undesired phase shifts between p- and s-polarized light. Because the phase shifts are nearly independent of the wavelength, i.e., the experimental results show no strong spectral tilt, they can be compensated by a suitable waveplate. The phase shifts accumulated between the LC-SLM and the photoelectron imaging spectrometer are corrected by a Berek-compensator. The measurement results of the polarization state analysis after correction of the detected phase shifts are displayed in Fig. 6(c). The results for horizontal and vertical polarization are unaffected, whereas the spectra measured for circularly polarized light are essentially constant demonstrating the successful compensation of the phase shifts. In order to assess the influences of the measured transmission spectrum of the pulse shaper, the phase shifts between p- and s-polarized components and the Berek-compensator characteristics on the resulting pulse shapes, we performed numerical simulations taking all these effects into account. These simulations show that the residual amplitude and phase effects can be neglected for the current state of sophistication

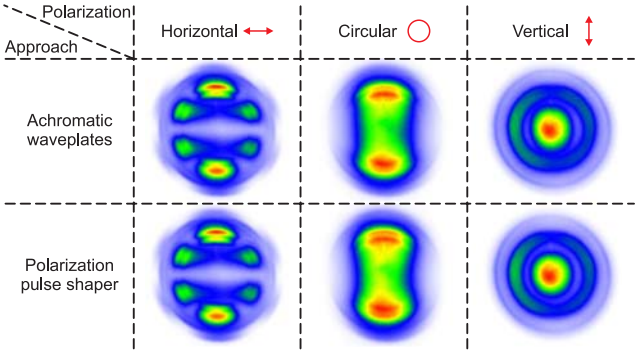

Fig. 7 Measured PADs from excitation of potassium with femtosecond laser pulses being in different states of polarization. The pulses were generated using two different methods: achromatic waveplates (*upper row*) and the polarization pulse shaper (*lower row*). The agreement between both approaches is excellent

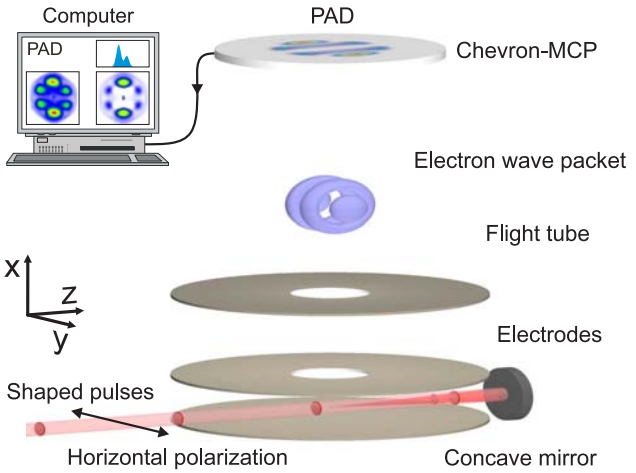

Fig. 8 Schematic diagram of the photoelectron imaging spectrometer. Shaped femtosecond laser pulses are focussed into the interaction region located within an electrode setup capable of "velocity-map imaging." The evolving three-dimensional electron wave packet is projected onto a double-MCP detector. The measured PADs are stored and processed in a computer system

justifying the three–dimensional visualizations of shaped pulses in Figs. 11 and 12 (cf. Sect. 4).

Finally, in order to verify the polarization shaping capabilities of our pulse shaper, a performance test on a real quantum system was carried out. As described in Sect. 2.4.2, PADs from REMPI provide a highly sensitive probe for polarization state analysis. In the first step the three polarization states mentioned above were realized by the use of achromatic waveplates. The upper row of Fig. 7 shows the corresponding measured PADs. Back-to-back we removed the waveplates and generated the different polarization states by the use of our polarization pulse shaper (including the Berek-compensator). The PADs resulting from excitation of potassium atoms using the shaper are presented in the lower row of Fig. 7. A comparison of the two approaches—waveplates vs. polarization pulse shaper—reveals excellent agreement proving in particular the pulse shaper's capability to accurately generate very complex polarization-shaped laser pulses in the interaction region of the imaging spectrometer. Note that no fine tuning of the pixel phases needed to be applied, in order to achieve these results.

3.3 Photoelectron imaging spectrometer

The experimental setup of the imaging spectrometer is shown schematically in Fig. 8. Femtosecond laser pulses generated by an amplified laser system (Femtolasers Femtopower Pro, 1 kHz, 30 fs, 1 mJ) and modulated by using either achromatic waveplates (B. Halle, $\lambda/2$, $\lambda/4$) or the polarization pulse shaper were focussed into potassium vapor supplied by an alkali metal dispenser source. Orientation of the crystal axes of the waveplates in relation to both the laser polarization and the photoelectron imaging spectrometer is ensured by using appropriate polarizers and a powermeter. The $\lambda/2$-waveplate is used to rotate the polarization axis (simulated in upper panels of Fig. 3, measured in upper panels of Fig. 10), the $\lambda/4$-waveplate is used to change the ellipticity of the laser pulses (simulated in lower panels of Fig. 3, measured in lower panels of Fig. 10). In order to achieve strong field conditions, we use an $f = 50$ mm focussing mirror to obtain intensities up to 5×10^{12} W/cm^2 for the bandwidth-limited laser pulse. The evolving three-dimensional electron wave packet is projected onto a position-sensitive detector using the "velocity-map imaging" method [61–64]. The detector consists of a double Multi-Channel Plate (MCP) in Chevron configuration and a phosphor screen deposited on a fiber optic. The signal from the phosphor screen is imaged with a 1.4 million pixel 10 bit CCD-camera (*Lumenera Corporation*). The signal-to-noise ratio of the images is increased by using one to four minutes time-integration of the signal in a computer. For linearly polarized light, the free-photoelectron wave packets are cylindrically symmetric with respect to the laser polarization. If the polarization is parallel to the detector plane, the three-dimensional angular distribution can be reconstructed from the PAD by Abel-inversion. Among the algorithms developed to perform the inversion [65–67], we use an adapted version of the pBasex-algorithm [68], which concentrates noise towards the center of the image.

Energy calibration of the spectrometer is performed by ionizing xenon atoms using the third harmonic of an ns-Nd:YAG laser system in a $3 + 1$ REMPI process. The achieved resolution is better than 50 meV FWHM at 1 eV.

4 Results and discussion

In this section we present experimental results obtained by excitation of potassium atoms with intense ultrashort laser pulses of various shapes and polarization states. To this end,

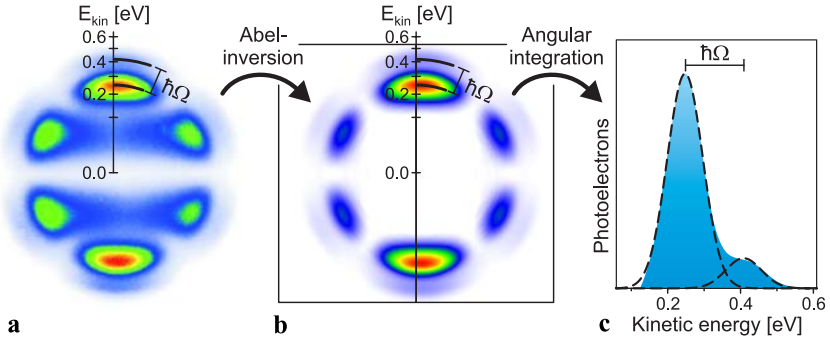

Fig. 9 (**a**) Measured and energy calibrated PAD from excitation with a linearly polarized (along the y-axis) pulse reveals $|f, m = 0\rangle$ symmetry of the photoelectron wave packet. (**b**) *Left half* of the image: PAD reconstructed from the measured image by Abel-inversion. *Right half* of the image: comparison to calculated section of the electronic wave packet in the y–z-plane from nonresonant strong-field excitation. (**c**) By angular integration of the reconstructed PAD energy resolved photoelectron spectra are obtained. The AT-splitting of $\hbar\Omega$ is depicted in all three graphs. Because the laser is slightly detuned from the atomic resonance, the lower dressed state is populated more efficiently visible by the pronounced peak of the photoelectrons with *low* kinetic energy. *Dotted lines* in (**c**) represent Gaussian fits of the two AT-components at $E_{\text{low}} = 248.7$ meV and $E_{\text{high}} = 409.3$ meV

we first dwell on the basic PAD measured upon excitation with an *unshaped* linearly polarized laser pulse. In this context, applications to tomography of atomic orbitals by rotation of the polarization axis are discussed. Next, we introduce V- and U-type spectral phase modulation functions to produce phase-only and complex polarization-shaped laser pulses, respectively. The resulting PADs exhibit arbitrarily complex structures, demonstrating the ability to specifically tailor the shape of free-electron wave packets by controlling coherent superpositions of contributing orbitals via the intense shaped light-field. Applications to generation and detection of electronic ring currents are presented in addition.

4.1 Energy distributions

At first, we focus on the kinetic energy dependence, i.e., the radial distribution of the measured photoelectron spectra. Figure 9(a) shows a measured PAD from excitation with an unshaped laser pulse linearly polarized along the y-axis. Note that the small left–right asymmetry in the PADs is related to the bias angle of the used MCP-detector and the different impact angles of photoelectrons. Application of the Abel-inversion yields the reconstructed electron wave packet displayed in the left half of Fig. 9(b). In the right half of Fig. 9(b) the result from the numerical simulation is presented, nicely matching the measurement. Considering the $p \leftrightarrow s$ excitation and $f \leftarrow\!\leftarrow p$ ionization step *in the atomic frame*, only $\Delta m = 0$ transitions are allowed in each step, and therefore an $|f, m = 0\rangle$ symmetry is observed. Due to the AT-effect (see Sect. 2.4.1), the radial distribution exhibits a double-ring structure indicating the highly nonperturbative population dynamics induced by the intense ultrashort laser pulse. The observed AT-splitting of $\hbar\Omega \approx 160$ meV arises from Rabi-cycling in the resonant neutral $p \leftrightarrow s$ system at the Rabi-frequency of $\Omega \approx 0.25$ rad/fs, which (in this case) corresponds to an intensity of 5×10^{10} W/cm^2. An elucidative picture of the excitation/ionization process is given in terms of dressed atomic states, i.e., the instantaneous eigenstates of the interacting light-atom-system [52]. Presence of a strong laser field lifts the degeneracy of the dressed state system such that the corresponding eigenenergies split up proportional to the Rabi-frequency $\Omega(t)$. Since ionization of the atom is triggered simultaneously, i.e., by the same laser field, the dressed state system rather than the bare state system is probed and mapped into the continuum. Thus, the AT-splitting directly measures the energy splitting of dressed states. Furthermore, the relative yield of the two AT-components reflects the *population* of either dressed state. In this picture, the asymmetry of the measured AT-doublet—as obtained by angular integration of the PAD (cf. Fig. 9(c))—in favor of low energetic photoelectrons is attributed to a preferential population of the lower dressed state during the interaction process resulting from the red-detuning of our laser spectrum with respect to the atomic resonance [40].

4.2 Polarization dependence

In this section, we discuss the experimental PADs obtained by excitation with a bandwidth-limited but specifically polarized ultrashort laser pulse. Figure 10 shows the measured PADs and parametric plots of the electric field vector $\hat{\boldsymbol{\epsilon}}(t) = \{\mathcal{E}_x(t), \mathcal{E}_y(t)\}^T$ in the x–y-plane to visualize the polarization properties of the pulse in the laboratory frame. Since the PADs are projections of the free-electron wave packets onto the MCP-plane (in the x-direction) iso-surfaces of the three-dimensional wave packets obtained by the simulation described in Sect. 2.3.3 are plotted along with the *measured* PADs (parallel to the y–z-plane). These graphs provide an intuitive interpretation of the measured PADs

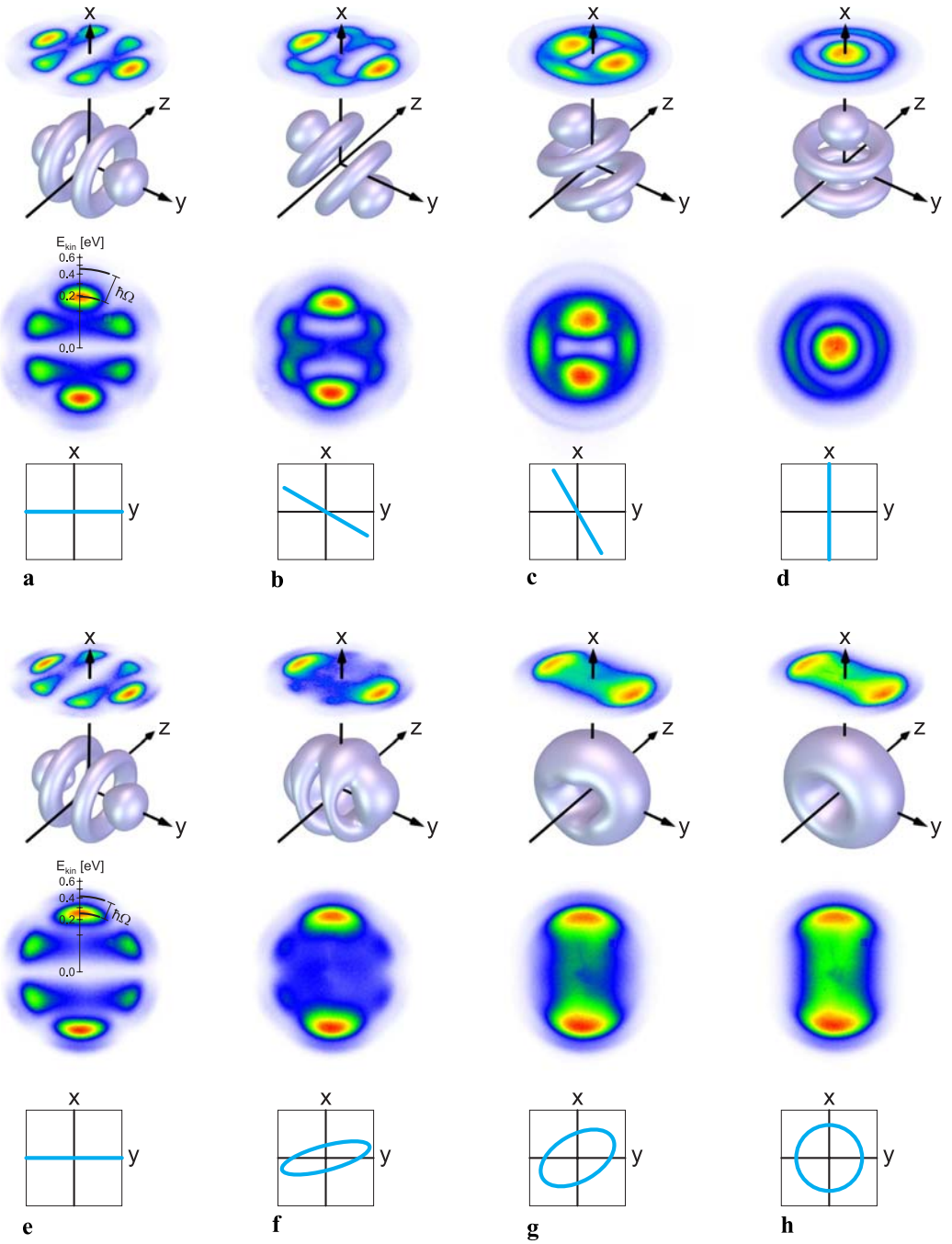

Fig. 10 Measured photoelectron angular distributions. The energy calibration is shown in (**a**). Parametric plots of the electric field in the x–y-plane indicate the polarization of the light pulses. The isosurfaces of the three-dimensional free-electron wave packets from the simulation link the polarization properties of light to the observed PADs—shown again as projection in the three-dimensional plot. *Upper panels*: linearly polarized light rotated about the z-axis by using a $\lambda/2$ plate whose optical axis is oriented at angles of 0°, 15°, 30°, and 45° with respect to the y-axis (compare to the simulated PADs in Fig. 3(a)–(d)). *Lower panels*: elliptically polarized light is produced by introducing a $\lambda/4$ plate with retardation axis oriented at 0°, 15°, 30°, and 45° with respect to the y-axis (compare with the simulated PADs in Fig. 3(f)–(h))

and reveal the underlying physical mechanisms to generate shaped electron wave packets. The PADs measured for linearly polarized pulses with different angles of the polarization vector in the x–y-plane are displayed in the upper panels of Fig. 10. As seen in the parametric plots, the polarization vector of the linearly polarized light rotates about the z-axis by 0, 30°, 60°, and 90°. In the experiment this was implemented by using an achromatic $\lambda/2$ plate with retarda-

tion axis oriented at angles of (a) 0°, (b) 15°, (c) 30°, and (d) 45° with respect to the y-axis. In Fig. 10(a) the polarization is parallel to the y-axis. Transformation into the *atomic frame* provides a conceptually simple way to understand the shape of this wave packet. Since linearly polarized light gives rise to $\Delta m = 0$ transitions, the REMPI process proceeds via the $|d, m = 0\rangle \leftarrow |p, m = 0\rangle \leftarrow |s, m = 0\rangle$ transitions to produce free-electron wave packets of $|f, m = 0\rangle$ symmetry. Physically, it is clear that rotation of the linear polarization in the laboratory frame rotates the orientation of the electron wave packet in the laboratory frame, i.e., the shape of the electron wave packet follows the state of polarization as shown in Fig. 10(a)–(d). Therefore, the PADs picture the transition from projecting the wave packet perpendicular to the atomic symmetry axis (a) to projecting it along to the symmetry axis *in the atomic frame* (d). In the latter case, the full rotational symmetry of the PAD reflects the rotational symmetry of the electron wave packet. Note that in the theoretical description, it is more consistent to describe the effect of linearly polarized light at different angles by the relative phase between two circularly polarized components using a different quantization axis (see Sect. 2). The agreement with the PADs obtained by simulation for the same states of polarization shown in Fig. 3(a)–(d) is excellent. The results presented in Fig. 10(a)–(d) imply the possibility to reconstruct three-dimensional wave packets by the measurement of PADs using polarization-shaped light pulses. Rotating a complex polarization-shaped pulse about the z-axis, for instance, with the help of a polarization pulse shaper, will rotate the complex-shaped wave packet and thus provides all the required projections for tomographic reconstruction. Experiments along these lines using polarization-shaped femtosecond laser pulses are presently carried out in our labs [69]. This technique will be useful for the reconstruction of electronic wave packets currently employed to characterize attosecond pulses and for studies of attosecond laser-induced electron wave packet dynamics mapped by PADs [70]. The lower panels of Fig. 10 reveal the effect of elliptically polarized laser pulses on PADs. In the experiment elliptically polarized light was produced by introducing a $\lambda/4$-plate and setting the angle of its retardation axis to (e) 0°, (f) 15°, (g) 30°, and (h) 45° with respect to the y-axis. In (e) the ellipse is degenerate, and therefore, the PAD agrees with the case of linear polarization depicted in (a). As the polarization changes from linear (e) to circular (h), the corresponding wave packets morph from the $|f, m = 0\rangle$ symmetry *in the atomic frame* to a toroidal shape with $|f, m = \pm 3\rangle$ symmetry. In general $|l, m = \pm l\rangle$ states are relevant to atomic ring currents as discussed in Sect. 4.5. Elliptically polarized light employed in the intermediate cases (f) and (g) produces complex-shaped wave packets mapped by peculiar PADs. Comparison of the measured and simulated PADs in Fig. 3(f)–(h) shows again excellent agreement. In the context of coherent control the ellipticity of light serves as a control parameter to manipulate the multipath interference of angular momentum states for effective quantum state engineering.

4.3 Linearly polarized shaped pulses

In this section we present PADs from excitation of potassium atoms with linearly polarized (along the y-axis) laser pulses which are phase-shaped in frequency domain. To this end, a V-type spectral phase modulation function of the form

$$\varphi_V(\omega) = \tau \cdot |\omega - \omega_V| \tag{12}$$

is introduced as a tool to generate double-pulse sequences with a pulse separation of 2τ. According to the Fourier shift theorem [71], this type of phase modulation shifts the low-frequency part of the spectrum, i.e., spectral components with $\omega < \omega_V$, in time by $-\tau$, whereas the remaining part of the spectrum with $\omega \geq \omega_V$ is shifted in time by $+\tau$. Assuming $\tau > 0$, this procedure results in a colored double-pulse sequence [72, 73]: an initial red-detuned pre-pulse followed by a blue-detuned post-pulse. By changing the sign of the parameter τ in (12) the progression of the pulses is reversed: a blue-detuned pre-pulse precedes a red-detuned post-pulse, two examples of which are depicted in

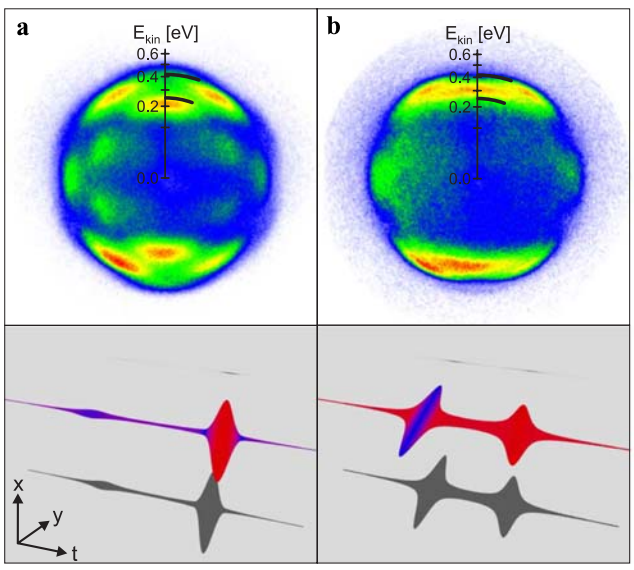

Fig. 11 *Upper panels*: measured PADs from excitation with linearly polarized phase-shaped laser pulses of 280 nJ pulse energy. *Lower panels*: three-dimensional visualization of the shaped pulses in the laboratory frame. Note that the time axis corresponds to the *negative* z-axis. (**a**) the spectral phase function $\varphi_V(\omega) = -200$ fs $\cdot\, |\omega - 2.44$ fs$^{-1}|$ generates a weak blue-detuned pre-pulse followed by an intense red-detuned post-pulse separated by 400 fs, whereas (**b**) the spectral phase function $\varphi_V(\omega) = -200$ fs $\cdot\, |\omega - 2.36$ fs$^{-1}|$ generates a blue-detuned pre-pulse followed by a red-detuned post-pulse of almost equal intensity

the lower panels of Fig. 11 in the fashion of [14]. Because both partial spectra are truncated, the resulting sub-pulses are much longer than the bandwidth-limited pulse. Shifting the cusp at ω_V away from the central frequency controls the share for both partial spectra and hence the intensity of the respective components. In Fig. 11 the projections of the pulses onto the x–z-plane vanish indicating linear polarization along the y-axis. The upper panels of Fig. 11 show PADs measured for such linearly polarized colored double pulses with (a) $\varphi_V(\omega) = -200\ \text{fs} \cdot |\omega - 2.44\ \text{fs}^{-1}|$ and (b) $\varphi_V(\omega) = -200\ \text{fs} \cdot |\omega - 2.36\ \text{fs}^{-1}|$, respectively. Since the central laser frequency in these experiments was $\omega_0 = 2.37\ \text{fs}^{-1}$, Fig. 11(a) corresponds to a very weak blue-detuned 135 fs pre-pulse followed by a strong red-detuned 50 fs post-pulse, whereas in Fig. 11(b) both pulses have approximately the same detunings, nearly the same intensity, and identical pulse lengths of 80 fs. All pulse durations given here are FWHM values resulting from 30 fs input pulses. As a result, the PAD shown in (a) clearly contains the previously discussed $|f, m = 0\rangle$ symmetry (cf. Fig. 9), while there is no evidence for this feature in (b). Most strikingly, the *angular* distribution of both PADs is different compared to the bandwidth-limited case. From the discussion in Sect. 2.4.1 it is expected that (weak- and strong-field) effects due to shaping linearly polarized pulses show up in the radial distribution of the PADs and not in changes of the angular distribution. The observed drastic changes in the *angular* distribution are therefore indeed surprising. A refined model to understand the detailed physical mechanism to generate PADs of the observed symmetries by linearly polarized shaped pulses is currently developed and will be presented in a forthcoming publication. As for the radial distribution, an additional ring shows up in both PADs at $E_{\text{kin}} \approx 0.4$ eV. This feature was not observed in the PAD from unshaped pulses (cf. Fig. 10).

4.4 Polarization-shaping

For excitation with polarization-shaped laser pulses, we use colored triple-pulse sequences. Analogous to the V-type spectral phase function mentioned in the previous section, these pulses are generated by dividing the spectrum into three regions $\omega \in \mathcal{R} = (-\infty, \omega_{V_1})$, $\omega \in \mathcal{C} = (\omega_{V_1}, \omega_{V_2})$ and $\omega \in \mathcal{B} = (\omega_{V_2}, \infty)$, where $\mathcal{R}$, $\mathcal{C}$, and $\mathcal{B}$ refer to the red, central, and blue parts of the spectrum, respectively. By applying a linear phase function to each of the spectral regions according to

$$\varphi_U(\omega) = \tau \cdot |\omega - \omega_{V_1}| + \tau \cdot |\omega - \omega_{V_2}|, \tag{13}$$

it is possible to shift their temporal counterpart by twice the respective time τ to produce colored triple-pulse sequences. However, similar to the V-shaped spectral phase, in this U-shaped spectral phase, the three spectral regions

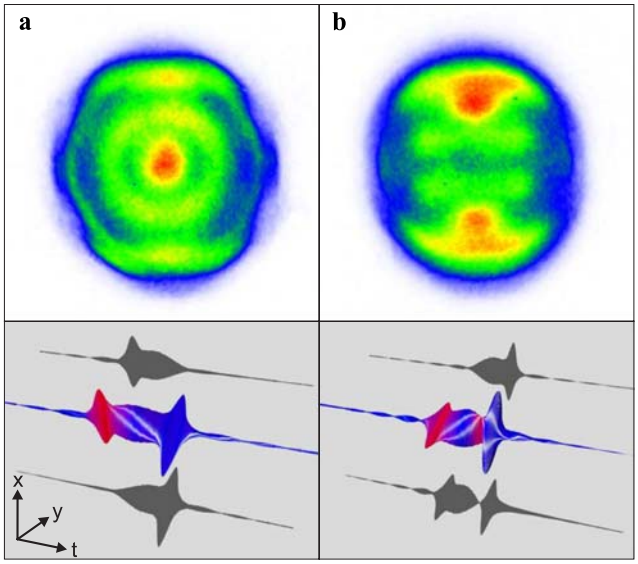

Fig. 12 *Upper panels*: measured PADs from excitation with polarization-shaped laser pulses of 8.0 μJ pulse energy. Three different linear phases are used to shift parts of the spectrum in time and create colored triple pulses, while also the polarization of these three spectral domains is changed. *Lower panels*: visualization of the polarization-shaped pulses: (**a**) the red-detuned pre-pulse is polarized along the x-axis, the central frequency components are left-elliptically polarized and the blue-detuned post-pulse is polarized along the y-axis, (**b**) the red-detuned pre-pulse is polarized along the y-axis, the central frequency components are left-elliptically polarized and the blue-detuned post-pulse is right-elliptically polarized

are sharply truncated, and therefore, the corresponding temporal slices are long and strongly overlapping. In order to design polarization-shaped pulses, the red spectral region $\mathcal{R}$ is advanced, the central spectral region $\mathcal{C}$ not shifted, and the blue spectral region $\mathcal{B}$ retarded for both polarization components. However, by adding absolute spectral phases with opposite signs of $\pm\pi/4$ to the phase of individual spectral regions given by (13) for both polarization components, the polarization of each spectral, and hence also each temporal slice is either left or right circularly polarized. In the same way, adding absolute spectral phases of 0 or $\pm\pi/2$ yields linearly polarized light along the y- or x-axis, respectively. For instance, the pulse depicted in Fig. 12(a) starts with a red-detuned pre-pulse linearly polarized along the x-axis, develops then into a left-elliptically polarized slice at the central-frequency to end up with a blue-detuned portion linearly polarized along the y-axis. The projections of the pulse onto both the x–z-plane and the y–z-plane show nonvanishing contributions, indicating polarization-shaping. In particular, the development from polarization along the x-axis, via elliptical polarization into polarization along the y-axis is visible in the projections. The pulse shown in Fig. 12(b) has a red-detuned pre-pulse polarized along the y-axis, changes to a left-elliptically polarized part, and concludes with a blue-detuned right-elliptically polarized part. The sub-pulse

durations are nearly the same for both pulses in Fig. 12. The central temporal slices have a length of about 300 fs FWHM, while both the pre-pulses and the post-pulses have a duration of about 100 fs FWHM. Again, these pulse durations result from 30 fs input pulses. The observed PADs exhibit very complex structures due to an entangled effect of strong-field excitation and polarization-shaping. Therefore the results cannot be easily interpreted in terms of the wave packets shown in Fig. 10. However, the results show that intense polarization-shaped REMPI opens a route to generate controllable photoelectron distributions with highly structured radial and angular components. The examples show that the use of intense polarization-shaped laser fields extends the degree of attainable control far beyond that obtained by single-parameter control discussed in Sects. 4.1 and 4.2.

4.5 Electronic ring currents

Recently, theoretical studies on the design of femtosecond laser pulses in order to generate electronic ring currents in atoms and molecules have received much interest [47, 74–76] motivated amongst other things by the potential of this technique to produce magnetic fields of unprecedented strength. In particular, the characteristics of laser pulses are so chosen as to selectively excite atomic and molecular (superposition) states maximizing the attainable magnetic field. Stationary ring currents in atoms were produced by excitation of $|l, m = l\rangle$, states, whereas nonstationary ring currents, for instance, in larger molecules, result from the excitation of superposition states. Now we present results on the generation and observation of coherent excitation of superpositions of the $|s, m = 0\rangle$ and the $|p, m = \pm 1\rangle$ states by circularly polarized pulses giving rise to nonstationary ring currents. As shown in Fig. 13, pulsed coherent excitation with right-handed circularly polarized light induces electronic dynamics on two different time scales. On the time scale ΔT of the pulse envelope, Rabi-oscillations of the population between the $|s, m = 0\rangle$ and the $|p, m = -1\rangle$ states occur within the time duration $T_R < \Delta T$. These Rabi-oscillations are observed in the AT-splitting of $\hbar\Omega \approx 2\pi\hbar/T_R$ in the photoelectron spectra (cf. Fig. 9 and [24, 30]). In addition, on the time scale of the optical cycle of the driving laser field T_0, the electronic wave packet rotates counter-clockwise about the z-axis. The red dots in the electric field depicted in Fig. 13 indicate instants separated by a quarter of an optical cycle $T_0/4 \approx 660$ as. The population of the excited $|p, m = -1\rangle$ state at these instances is shown by the black dots in the upper panel of Fig. 13. The dynamics of the electronic wave packet at these instances is depicted in the magnification of a single optical cycle in the lower panel of Fig. 13. Because the nonstationary electronic ring current oscillates at the Bohr-frequency resonant with the exciting laser frequency, the nonstationary nature of this process

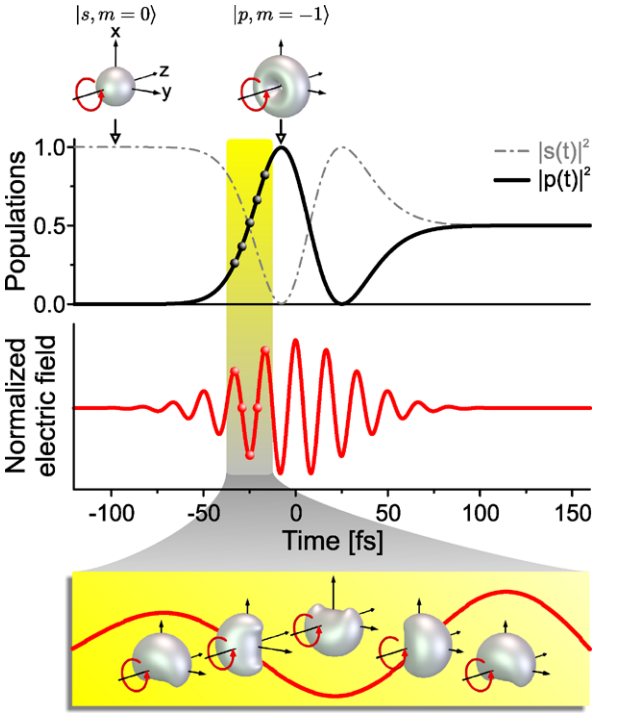

Fig. 13 Coherent excitation of superpositions of the $|s, m = 0\rangle$ and the $|p, m = -1\rangle$ states by right-handed circularly polarized pulses (shown as projection in the *middle panel*) gives rise to dynamics on two different time scales. (1) Rabi-oscillations of the population between these two states on the time scale of the pulse envelope give rise to the observed AT-splitting in the photoelectron spectra. (2) Within an optical cycle of the driving laser field the electronic wave packet rotates about the z-axis in a counter-clockwise sense yielding a nonstationary electronic ring current (see magnification of a single optical cycle in the *lower panel*)

cannot be directly mapped by a laser pulse at the same frequency. However, the measured toroidal shape of the PAD in Fig. 10(h)—indicative of the time–averaged nonstationary ring current—together with the AT-splitting—indicative of Rabi-oscillations (cf. Sect. 4.1)—provide experimental evidence of PADs resulting from a nonstationary ring current as illustrated in the lower panel of Fig. 13. The simpler task to excite a stationary ring current is accomplished by coherent excitation of a $|p, m = \pm 1\rangle$ state using a circularly polarized π-pulse. Experimentally, stationary ring currents were achieved by reducing the laser intensity such that the pulse area approaches π. Direct time-resolved observations of nonstationary electronic ring currents are within reach employing currently available femtosecond-pump and attosecond-probe techniques [77].

5 Conclusions

In the recent past Photoelectron Angular Distributions (PADs) have proven to be essential to analyze ionization dynamics [78] and (neutral) molecular dynamics [79] because

they contain highly differential information. Progress has also been made in controlling the ionization rate of molecules, i.e., a scalar quantity, by polarization-shaped laser pulses [20]. In the present work we have extended the scope of these observations and have demonstrated that detection of PADs is an adequate technique to attack intrinsically three-dimensional quantum control tasks by direct mapping the structure of three-dimensional wave packets.

So far, the use of linearly polarized light is regarded a basic prerequisite for the application of velocity map imaging techniques and in particular for the interpretation of measured PADs. However, in order to achieve three-dimensional quantum control by employing polarization-shaped laser pulses, it is required to generalize this principle. In this case, the interpretation of the measured PADs in terms of the underlying dynamics requires theoretical modeling as shown on our model system, i.e., for Resonance Enhanced Multi-Photon Ionization (REMPI) of atoms with elliptically polarized light. On the other hand, elaborate use of the polarization properties of light can reveal additional information exploiting the fact that PADs are projections of (in general) complex-shaped wave packets. Measurements of PADs by rotating the complex polarization-shaped laser pulse deliver all information required for tomographic techniques to reconstruct the electron wave packets. With this technique controlled complex-shaped three-dimensional electron wave packets are accessible to direct measurements [69].

In this work, we have exerted control on the dynamics of neutral electronic wave packets by nonperturbative excitation and have controlled free-electron wave packets by manipulating the ionization step. We have shown that by tailoring the state of polarization, a high degree of control on the angular distributions of ultrashort free-electron wave packets is obtained by interference of multiple excitation and ionization pathways. A theoretical description of PADs obtained by nonperturbative REMPI with ultrashort polarization-shaped laser pulses has been presented and compared to experimental results.

Combining the additional dimensions provided by strong fields and by control of the instantaneous state of polarization will open new perspectives for coherent control by tailored quantum state engineering due to the unprecedented options for spatial control. As an example, the measured toroidal shape of the PAD obtained upon excitation with circularly polarized light pulses together with the nonperturbative nature of the excitation process provides experimental evidence for the observation of nonstationary electronic ring currents. Observation by PADs being highly sensitive to the electronic structure and dynamics is a key to obtain the required differential information to fully explore the power of three-dimensional coherent control also on larger systems. The interpretation of experimental PADs from ionizing larger molecules with polarization-shaped laser pulses in terms of molecular dynamics will present major challenges to quantum chemists. Currently experiments to extend this approach to larger molecules are being carried out in our labs.

Acknowledgements The financial support by the Deutsche Forschungsgemeinschaft DFG and the EU Marie Curie initial training network FASTQUAST is gratefully acknowledged.

References

1. A. Weiner, Rev. Sci. Instrum. **71**, 1929 (2000)
2. M. Wollenhaupt, A. Assion, T. Baumert, in *Springer Handbook of Lasers and Optics* (Springer, Berlin, 2007)
3. T. Baumert, J. Helbing, G. Gerber, in *Advances in Chemical Physics* (Wiley, New York, 1997)
4. A. Assion et al., Science **282**, 919 (1998)
5. S.A. Rice, M. Zhao, *Optical Control of Molecular Dynamics* (Wiley, New York, 2000)
6. M. Shapiro, P. Brumer, *Principles of the Quantum Control of Molecular Processes* (Wiley, New York, 2003)
7. D. Tannor, *Introduction to Quantum Mechanics: A Time-Dependent Perspective* (University Science Books, Herndon, 2006)
8. H. Rabitz, R. de Vivie-Riedle, M. Motzkus, K. Kompa, Science **288**, 824 (2000)
9. R.J. Levis, H.A. Rabitz, J. Phys. Chem. A **106**, 6427 (2002)
10. M. Dantus, V.V. Lozovoy, Chem. Rev. **104**, 1813 (2004)
11. M. Wollenhaupt, V. Engel, T. Baumert, Annu. Rev. Phys. Chem. **56**, 25 (2005)
12. T. Brixner et al., in *Femtosecond Laser Spectroscopy* (Springer, Berlin, 2005)
13. H. Fielding, M. Shapiro, T. Baumert (eds), J. Phys. B **41** (2008). Special Issue on Coherent Control
14. T. Brixner, G. Gerber, Opt. Lett. **26**, 557 (2001)
15. L. Polachek, D. Oron, Y. Silberberg, Opt. Lett. **31**, 631 (2006)
16. M. Plewicki, F. Weise, S.M. Weber, A. Lindinger, Appl. Opt. **45**, 8354 (2006)
17. M. Plewicki, S.M. Weber, F. Weise, A. Lindinger, Appl. Phys. B **86**, 259 (2007)
18. M. Ninck, A. Galler, T. Feurer, T. Brixner, Opt. Lett. **32**, 3379 (2007)
19. O. Masihzadeh, P. Schlup, R.A. Bartels, Opt. Express **15**, 18025 (2007)
20. T. Brixner et al., Phys. Rev. Lett. **92**, 208301 (2004)
21. N. Dudovich, D. Oron, Y. Silberberg, Phys. Rev. Lett. **92**, 103003 (2004)
22. T. Suzuki, S. Minemoto, T. Kanai, H. Sakai, Phys. Rev. Lett. **92**, 133005 (2004)
23. F. Weise, S.M. Weber, M. Plewicki, A. Lindinger, Chem. Phys. **332**, 313 (2007)
24. M. Wollenhaupt et al., Phys. Rev. A **68**, 015401 (2003)
25. N. Dudovich, T. Polack, A. Pe'er, Y. Silberberg, Phys. Rev. Lett. **94**, 083002 (2005)
26. C. Trallero-Herrero, J.L. Cohen, T. Weinacht, Phys. Rev. Lett. **96**, 063603 (2006)
27. B.W. Shore, Acta Phys. Slov. **58**, 243 (2008)
28. T. Frohnmeyer, M. Hofmann, M. Strehle, T. Baumert, Chem. Phys. Lett. **312**, 447 (1999)
29. B.J. Sussman, D. Townsend, M.Y. Ivanov, A. Stolow, Science **314**, 278 (2006)
30. M. Wollenhaupt, A. Präkelt, C. Sarpe-Tudoran, D. Liese, T. Baumert, J. Opt. B **7**, 270 (2005)

31. M. Wollenhaupt, D. Liese, A. Präkelt, C. Sarpe-Tudoran, T. Baumert, Chem. Phys. Lett. **419**, 184 (2006)
32. E. Sleva, I. Xavier Jr., A. Zewail, J. Opt. Soc. Am. B **3**, 483 (1985)
33. Y. Bai, A. Yodh, T. Mossberg, Phys. Rev. Lett. **55**, 1277 (1985)
34. T. Bayer, M. Wollenhaupt, C. Sarpe-Tudoran, T. Baumert, Phys. Rev. Lett. **102**, 023004 (2009)
35. N.V. Vitanov, T. Halfmann, B.W. Shore, K. Bergmann, Annu. Rev. Phys. Chem. **52**, 763 (2001)
36. M. Wollenhaupt, T. Baumert, J. Photochem. Photobiol. A **180**, 248 (2006)
37. M. Wollenhaupt, A. Präkelt, C. Sarpe-Tudoran, D. Liese, T. Baumert, J. Mod. Opt. **52**, 2187 (2005)
38. M. Wollenhaupt et al., Phys. Rev. A **73**, 063409 (2006)
39. M. Wollenhaupt, A. Präkelt, C. Sarpe-Tudoran, D. Liese, T. Baumert, Appl. Phys. B **82**, 183 (2006)
40. T. Bayer, M. Wollenhaupt, T. Baumert, J. Phys. B **41**, 074007 (2008)
41. R. Selle, T. Brixner, T. Bayer, M. Wollenhaupt, T. Baumert, J. Phys. B **41**, 074019 (2008)
42. S. Zamith et al., Phys. Rev. Lett. **87**, 033001 (2001)
43. W. Salzmann et al., Phys. Rev. Lett. **100**, 233003 (2008)
44. M. Wollenhaupt et al., Phys. Rev. Lett. **89**, 173001 (2002)
45. T. Seideman, Annu. Rev. Phys. Chem. **53**, 41 (2002)
46. T. Suzuki, B.J. Whitaker, Int. Rev. Phys. Chem. **20**, 313 (2001)
47. I. Barth, J. Manz, Phys. Rev. A **75**, 012510 (2007)
48. B.H. Bransden, C.J. Joachain, *Physics of Atoms and Molecules* (Wiley, New York, 2003)
49. B.W. Shore, Act. Phys. Slov. **58**, 243 (2008)
50. I.V. Hertel, C.P. Schulz, *Atome, Moleküle und Optische Physik 1* (Springer, Berlin, 2008)
51. M. Winter, M. Wollenhaupt, T. Baumert, Opt. Commun. **264**, 285 (2006)
52. B.W. Shore, *The Theory of Coherent Atomic Excitation* (Wiley, New York, 1990)
53. E.A. Shapiro, V. Milner, C. Menzel-Jones, M. Shapiro, Phys. Rev. Lett. **99**, 033002 (2007)
54. U. Gaubatz et al., Chem. Phys. Lett. **149**, 463 (1988)
55. R. Kosloff, A.D. Hammerich, D. Tannor, Phys. Rev. Lett. **69**, 2172 (1992)
56. D. Tannor, R. Kosloff, A. Bartana, Faraday Discuss. **113**, 365 (1999)
57. National Institute of Standards and Technology, http://www.nist.gov
58. A. Präkelt et al., Rev. Sci. Instrum. **74**, 4950 (2003)
59. T. Brixner, G. Krampert, P. Niklaus, G. Gerber, Appl. Phys. B **74**, S133 (2002)
60. P. O'Shea, M. Kimmel, X. Gu, R. Trebino, Opt. Lett. **26**, 932 (2001)
61. D.W. Chandler, P.L. Houston, J. Chem. Phys. **87**, 1445 (1987)
62. C. Bordas, F. Paulig, H. Helm, D.L. Huestis, Rev. Sci. Instrum. **67**, 2257 (1996)
63. A.T.J.B. Eppink, D.H. Parker, Rev. Sci. Instrum. **68**, 3477 (1997)
64. B. Whitaker, *Imaging in Molecular Dynamics* (Cambridge University Press, Cambridge, 2003)
65. J. Winterhalter, D. Maier, J. Honerkamp, V. Schyja, H. Helm, J. Chem. Phys. **110**, 11187 (1999)
66. M.J.J. Vrakking, Rev. Sci. Instrum. **72**, 4084 (2001)
67. V. Dribinski, A. Ossadtchi, V.A. Mandelshtam, H. Reisler, Rev. Sci. Instrum. **73**, 2834 (2002)
68. G.A. Garcia, L. Nahon, I. Powis, Rev. Sci. Instrum. **75**, 4989 (2004)
69. M. Krug, M. Wollenhaupt, J. Köhler, T. Baumert, (2009 to be published)
70. J. Mauritsson et al., Phys. Rev. Lett. **100**, 073003 (2008)
71. R. Bracewell, *The Fourier Transform and Its Applications* (McGraw-Hill, New York, 2000)
72. M. Renard, R. Chaux, B. Lavorel, O. Faucher, Opt. Express **12**, 473 (2004)
73. G. Vogt et al., Phys. Rev. A **74**, 033413 (2006)
74. I. Barth, J. Manz, Angew. Chem. Int. Ed. **45**, 2962 (2006)
75. I. Barth, J. Manz, Y. Shigeta, K. Yagi, J. Am. Chem. Soc. **128**, 7043 (2006)
76. I. Barth, L. Serrano-Andrés, T. Seidemann, J. Chem. Phys. **129**, 164303 (2008)
77. M.F. Kling, M.J.J. Vrakking, Annu. Rev. Phys. Chem. **59**, 463 (2008)
78. U. Müller, H. Helm, in *Many Particle Quantum Dynamics in Atoms and Molecules* (Springer, Berlin, 2003)
79. A. Stolow, A.E. Bragg, D.M. Neumark, Chem. Rev. **104**, 1719 (2004)